

# Title

Inverse-designed lithium niobate nanophotonics

## Authors

Chengfei Shang,<sup>1†</sup> Jingwei Yang,<sup>1†</sup> Alec M. Hammond,<sup>2</sup> Zhaoxi Chen,<sup>1</sup> Mo Chen,<sup>3</sup> Zin Lin,<sup>4</sup> Steven G. Johnson,<sup>3\*</sup> and Cheng Wang<sup>1\*</sup>

## Affiliations

<sup>1</sup>Department of Electrical Engineering & State Key Laboratory of Terahertz and Millimeter Waves, City University of Hong Kong, Kowloon, Hong Kong, China

<sup>2</sup>School of Electrical and Computer Engineering, Georgia Institute of Technology, Atlanta, GA 30308, USA

<sup>3</sup>Department of Mathematics, Massachusetts Institute of Technology, Cambridge, MA 02139, USA

<sup>4</sup>Department of Electrical and Computer Engineering, Virginia Polytechnic Institute and State University, Arlington, VA 22203, USA

<sup>†</sup>These authors contributed equally to this article

\*[stevenj@math.mit.edu](mailto:stevenj@math.mit.edu)

\*[cwang257@cityu.edu.hk](mailto:cwang257@cityu.edu.hk)

## Keywords

Inverse design, topology optimization, lithium niobate, integrate photonics

## Abstract

Lithium niobate-on-insulator (LNOI) is an emerging photonic platform that exhibits favorable material properties (such as low optical loss, strong nonlinearities, and stability) and enables large-scale integration with stronger optical confinement, showing promise for future optical networks, quantum processors, and nonlinear optical systems. However, while photonics engineering has entered the era of automated “inverse design” via optimization in recent years, the design of LNOI integrated photonic devices still mostly relies on intuitive models and inefficient parameter sweeps, limiting the accessible parameter space, performance, and functionality. Here, we implement a 3D gradient-based inverse-design model tailored for topology optimization based on the LNOI platform, which not only could efficiently search a large parameter space but also takes into account practical fabrication constraints, including minimum feature sizes and etched sidewall angles. We experimentally demonstrate a spatial-mode multiplexer, a waveguide crossing, and a compact waveguide bend, all with low insertion losses, tiny footprints, and excellent agreement between simulation and experimental results. The devices, together with the design methodology, represent a crucial step towards the variety of advanced device functionalities needed in future LNOI photonics, and could provide compact and cost-effective solutions for future optical links, quantum technologies and nonlinear optics.

## Introduction

The lithium niobate-on-insulator (LNOI) platform has seen rapid development<sup>(1)</sup> in recent years and

shows great potential in future advanced photonics systems, owing to the excellent optical properties of lithium niobate (LN), including large nonlinear susceptibilities, a wide optical transparency window, and great stability, as well as strong optical confinement that allows compact and scalable integrated photonic devices and circuits to be built on wafer scales. A wide range of on-chip nanophotonic devices, including high-speed electro-optic modulators<sup>(2-4)</sup>, high-Q micro resonators<sup>(5,6)</sup>, broadband frequency comb generators<sup>(7-9)</sup>, efficient frequency convertors<sup>(10-13)</sup>, entangled photon pair generators<sup>(14)</sup>, spectrometer<sup>(15)</sup>, optical isolator<sup>(16)</sup>, ultrafast all-optical switches<sup>(17)</sup> and frequency shifters<sup>(18)</sup> have been demonstrated, making LN-based photonic integrated circuits a promising solution for future high-speed optical networks, quantum information processing, and nonlinear optics. However, to date the design of most LNOI devices still relies heavily on human intuition augmented by simple analytical models, and can only access limited parameter spaces by scanning a few hand-selected parameters (such as widths, gaps and radii of curvature), either manually or through inefficient parameter sweeps (whose cost scales exponentially with the number of parameters).

Inverse-design methods, also as known as topology optimization<sup>(19-20)</sup>, on the other hand, have been developed and attracted considerable attention in nanophotonics in the last two decades. Such methods could automatically search for the optimal topological structure of a pre-specified objective in a certain design region, exploring a large parameter space through meticulously developed optimization algorithms. Inverse design can reveal highly non-intuitive device designs with extremely compact sizes (several micrometers in diameter) and unprecedented functionalities. Many inverse-designed functional devices have been demonstrated in recent years, such as photonic crystal structures<sup>(21-23)</sup>, mode multiplexers and convertors<sup>(24,25)</sup>, wavelength multiplexers<sup>(26,27)</sup>, meta-surfaces<sup>(28,29)</sup>, nonlinear wavelength convertors<sup>(29-31)</sup>, dispersion-engineered microresonators<sup>(32,33)</sup>, together with system applications such as massively parallel optical transmitters<sup>(34)</sup>, particle accelerators<sup>(35)</sup>, and chip-based light detection and ranging (LiDAR) systems<sup>(36-37)</sup>.

Thus far, most inverse-designed photonic devices have been demonstrated in silicon (Si) and other CMOS-compatible platforms such as silicon nitride<sup>(28)</sup> because of the mature fabrication technologies available for those materials. Compared with Si photonics, the challenges in the design and implementation of inverse-designed LNOI devices mainly arise from practical fabrication constraints. Due to the difficulty in dry etching LN and electro-optic overlap considerations, typical waveguides in LNOI feature a rib structure with an unetched slab underneath, further reducing the already smaller effective index contrast compared with that of Si photonics. Moreover, dry-etched LNOI waveguides usually exhibit a substantial sidewall angle, which needs to be taken into consideration during the optimization process to achieve accurate modeling, and which also limits the minimally achievable feature sizes. More recently, inverse-design algorithms that take into account specific geometric constraints<sup>(38)</sup> and sidewall angles<sup>(39)</sup> have led to designs and demonstrations compatible with standard foundry services<sup>(42)</sup> and in more exotic material platforms such as diamond<sup>(43)</sup> and silicon carbide<sup>(33)</sup>. However, the realization of inverse-designed LNOI devices is still missing and could substantially benefit the development of compact LNOI photonic integrated circuits, especially when dealing with complex design problems with multiple objective figures of merit.

Here, we overcome these fabrication and design challenges and demonstrate a series of compact high-performance inverse-designed LNOI photonic devices based on the open-source Meep package<sup>(44)</sup>. The design algorithm takes into full consideration of the fabrication constraints in the

LNOI platform, including the rib structures, minimum feature sizes and etched sidewalls. We design and fabricate a spatial-mode multiplexer that separates the fundamental transverse-electric ( $TE_0$ ) mode and second-order TE ( $TE_1$ ) mode, with an insertion loss  $\sim 1.5$  dB and a crosstalk  $< -15.8$  dB, a waveguide crossing with a low loss of 0.48 dB and a crosstalk  $< -36$  dB, and a compact waveguide bend that turns the propagation of light by  $90^\circ$  with a radius of curvature of  $6\ \mu\text{m}$  and a loss of 0.41 dB. The devices show excellent agreement between theoretical and experimental performances, as well as broad operation bandwidths from 1500 nm to 1600 nm wavelength.

## Results

Figure 1(a) shows an overview of our inverse-design strategy specially tailored for the LNOI platform and a representative iteration curve. The inverse design relies on a hybrid time/frequency-domain topology-optimization algorithm<sup>(45)</sup> with adjoint sensitivity analysis and multiple constraint functions. Starting with a homogeneous design region (typically initialized to “gray”—halfway between air and LNOI) and a given objective function, e.g., the transmission coefficients of a particular waveguide mode, the optimization solver efficiently calculates the objective performance and the gradients in each iteration step by two FDTD (finite-difference time domain) simulations regardless of the number of pixelated design parameters. Compared with optimization problems in SOI, the slanted sidewalls in the LNOI platform require special optimization algorithm design, whereas the existence of an unetched slab substantially increases the difficulty in achieving good optimization performances due to a lowered effective-index contrast. In this paper we use a 400 nm z-cut LN device layer with a 250 nm etch depth and a sidewall angle of 45 degree for all designs (see device fabrication in supplementary information (S.I.)), similar to other devices previously demonstrated in our group<sup>(4,46)</sup>.

The optimization strategy shown in Fig. 1(a) contains three main steps as outlined in Ref. 45. In the first step, permittivity in the design region is allowed to vary continuously, while a convolution and projection function is introduced to smoothen the design region and improve the dynamic range. The projection strength  $\beta$  is increased gradually during the iterations to avoid a dramatic change in the design parameters, such that the optimizer focuses on improving the figure of merit while gradually pushing the design towards a more binarized permittivity distribution. In the second step, we incorporate a geometric constraint<sup>(38)</sup> to eliminate features smaller than the indicated minimum length scales, during which the design parameters are further binarized. Finally, we introduce sidewall features by using linearly shifted threshold values for the projection function at different vertical slices<sup>(39)</sup>, so that the pattern is “eroded” as a function of the height above the slab surface (Fig. 1(b)). In our simulations, we use a threshold value interval from 0.375 (bottom) to 0.625 (top), within which the length scale roughly changes linearly with the threshold according to previous studies<sup>(40,41)</sup> and our experience. In each step, the optimizer runs for several tens of iterations before convergence, the precise number depending on the specific problem. Importantly, all simulations are performed in 3D, taking fully into account the practical rib/slab thicknesses, crystal anisotropy, and sidewall angles, which are crucial to realize experimentally achievable designs. More mathematical details regarding the inverse design algorithms can be found in the device design section and Fig. S1 in S.I., as well as in previous references<sup>(38,39,47)</sup>. Figure 1(c-e) shows schematic views of the designed structures and their corresponding functions of our mode multiplexer, waveguide crossing and compact waveguide bend, respectively.

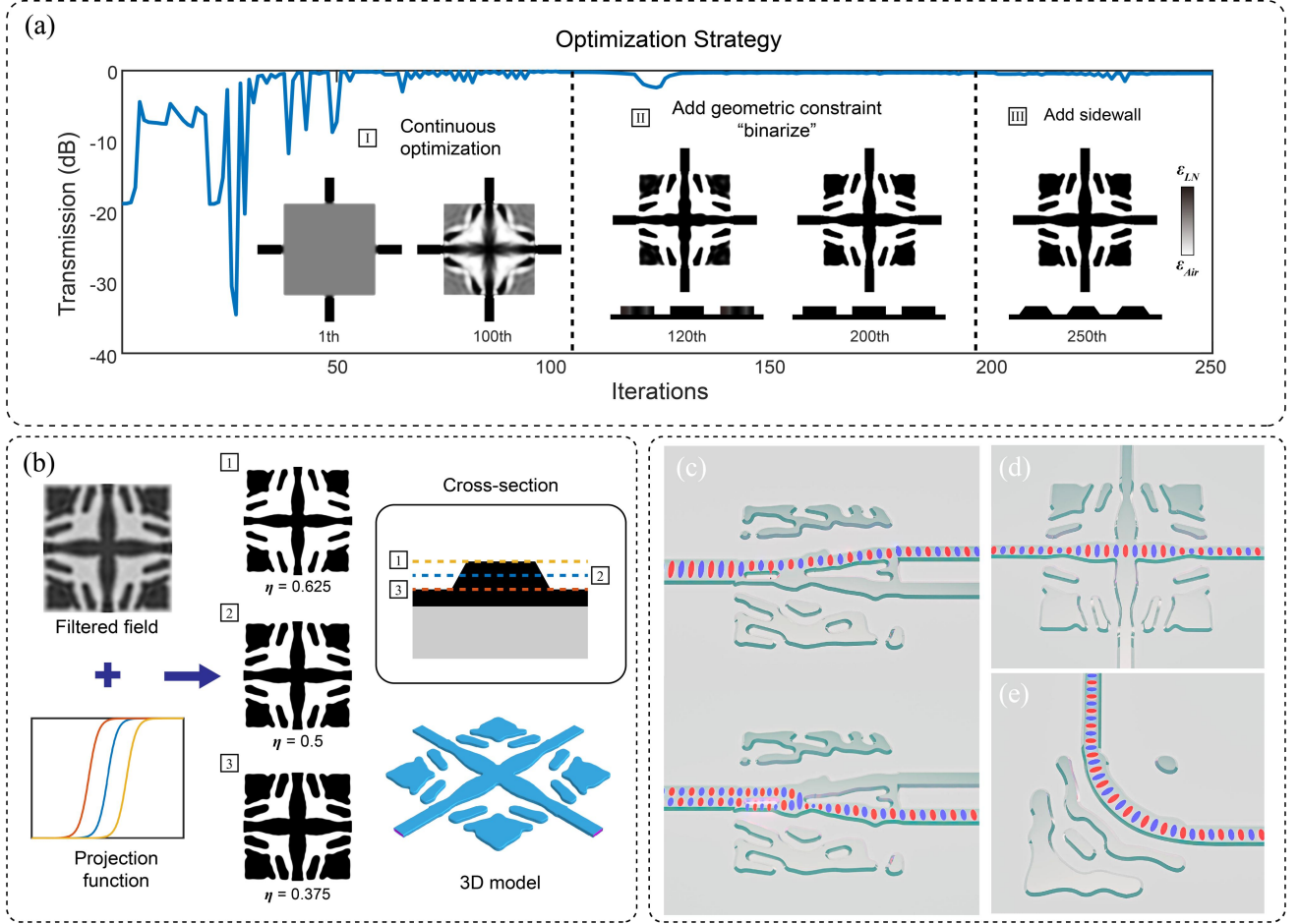


**Figure 1.** Overview of the optimization strategy and device schematic. (a) General optimization strategy and a typical iteration curve of a waveguide crossing optimization problem consisting of three main steps. In the first step, the permittivity in each pixel is allowed to vary continuously; second, we add geometric constraints to binarize the structure and achieve a minimum length scale; finally, slanted sidewall is introduced while the solver reoptimizes the design to “compensate” for the sidewall-induced performance degradation. The cross-section views in step 2 and step 3 are drawn along the diagonal of the design region. (b) Method of adding sidewall features. We introduce linearly shifted threshold values  $\eta$  for the hyperbolic tangent projection function at different heights (left), which leads to eroded ( $\eta = 0.625$ ), normal ( $\eta = 0.5$ ) and dilated ( $\eta = 0.375$ ) structures at the top, center and bottom slices of the rib structure, respectively (right). We design and fabricate (c) a  $TE_0/TE_1$  mode multiplexer, (d) a waveguide crossing, and (e) a compact waveguide bend to verify the design strategy, all of which show good performance and excellent fabrication compatibility.

### Spatial Mode Multiplexer

First, we consider an LNOI spatial mode multiplexer, an important component for mode-division multiplexing (MDM) technology in future high-volume data transmission systems<sup>(48)</sup>. In our design, the fundamental  $TE_0$  mode in a  $2\ \mu\text{m}$  wide input waveguide will be coupled into the upper output arm, whereas the  $TE_1$  mode will be converted into  $TE_0$  mode, and output from the bottom arm (Fig. 2(a)). The two output waveguides are both  $1\ \mu\text{m}$  wide and are separated by a  $2\ \mu\text{m}$  gap. Figure 2(a) shows the final inverse-designed pattern together with simulated field evolution ( $E_y$ ) for  $TE_0$  and  $TE_1$  input, whereas Figure 2(b) shows the scanning electron microscope (SEM) image of the fabricated mode multiplexer. The footprint of the final design is  $12 \times 12\ \mu\text{m}^2$ , orders of magnitude smaller compared with mode multiplexers based on traditional asymmetrical directional couplers (ADCs)<sup>(49)</sup> or cascaded Mach–Zehnder interferometers (MZI)<sup>(50)</sup>. The minimum feature size is set to be  $0.2\ \mu\text{m}$  (at the middle slice of the rib) to balance between the potential degrees of freedom in design and the

fabrication constraints. Our simulation results show that, for both  $TE_0$  and  $TE_1$  input scenarios, a single mode multiplexer features an average insertion loss less than 0.9 dB and crosstalk less than -17 dB over a 100-nm wavelength window (1500 nm-1600 nm). In our actual experiments, we fabricate two multiplexers back to back connected by a 50- $\mu\text{m}$ -long, 2- $\mu\text{m}$ -wide multimode waveguide, such that all input/output signals are in  $TE_0$  mode and are easier to be precisely calibrated. The simulation result (Fig. 2(c)) for such a cascaded mode multiplexer pair shows average insertion losses at the desired outputs ( $S_{31}$  and  $S_{42}$ ) of less than 2 dB (twice the loss of a single device), and crosstalk ( $S_{41}$  and  $S_{32}$ ) of less than -16.5 dB. In the experimental test (Fig. 2(d)), we measure average insertion losses of less than 3 dB and crosstalk less than -15.8 dB for the mode-multiplexer pair within a wavelength range between 1520 nm and 1600 nm, consistent with the simulation results. The measured insertion loss values are further corroborated by comparing the losses of two and four cascaded mode-multiplexers (see performance estimation in S.I.). From the results we estimate that a single mode multiplexer features an insertion loss  $\sim 1.5$  dB and an upper-bound crosstalk value of -15.8 dB within the 80-nm wavelength window (see performance estimation for a detailed analysis). The remaining differences between simulation and experimental values could result from excessive scattering losses due to deviations in the actually fabricated device parameters and fabrication imperfections especially on the small features (see origin of excessive insertion loss and Fig. S2 in S.I. for more details). We also note that the peripheral structures in our design (e.g. the top and bottom bars in Fig.2(a)) do not substantially contribute to the overall field evolution (Fig. S3 in S.I.), potentially allowing the achievement of similar device performances within even smaller footprints by adopting customized shapes of design region.

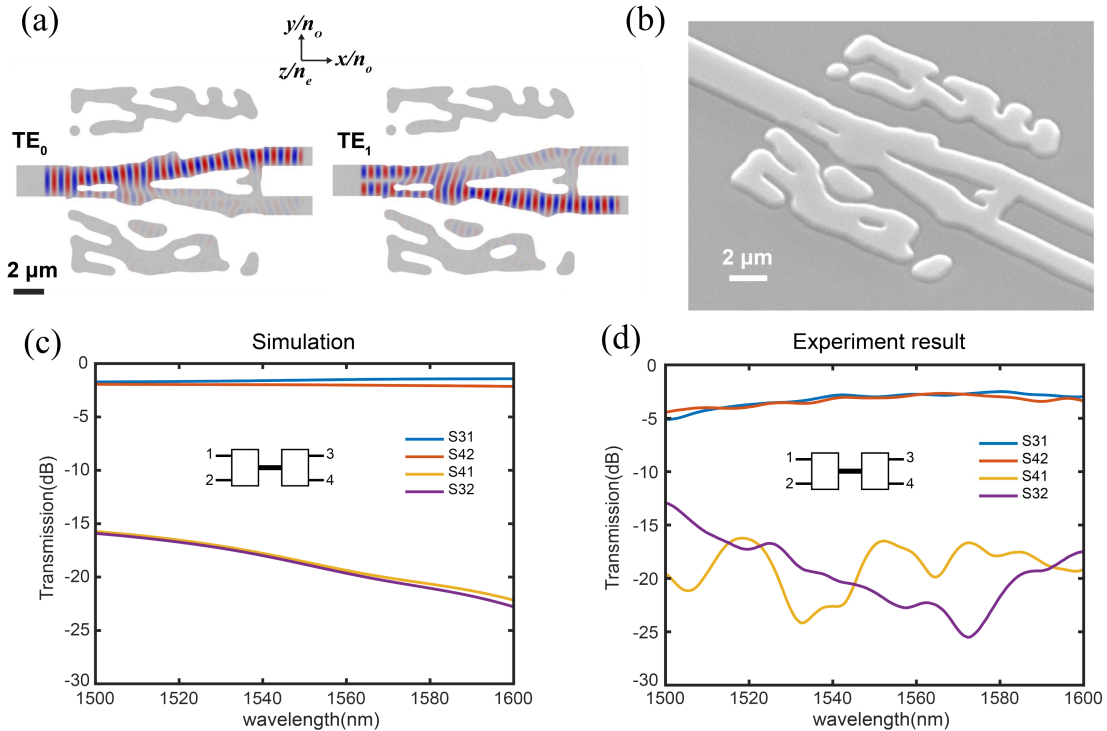


**Figure 2.** Inverse-designed spatial mode multiplexer. (a) The optimized design pattern and simulated field ( $E_y$ ) evolution of the mode multiplexer with a  $12 \times 12 \mu\text{m}^2$  footprint. The gray and white areas correspond to LN rib and slab regions, respectively. (b) SEM image of the fabricated mode multiplexer. (c) Simulated transmission coefficients of a back-to-back mode multiplexer pair between the four input/output ports as shown in the inset. (d) Experimentally measured transmission coefficients of a fabricated mode multiplexer pair, showing broadband low-loss and low-crosstalk operation consistent with simulation results.

## Waveguide crossing

A waveguide crossing<sup>(51-56)</sup> is an essential component for signal routing in large-scale and high-density photonic integrated circuits. Traditional waveguide crossing designs typically rely on heuristic shaped taper or multimode interferometer (MMI) structures combined with exhaustive parameter sweeps<sup>(54,55)</sup>. Here we design a compact waveguide crossing using our inverse-design algorithm without the need for an initial guess. The design region (Fig. 3(a)) again has a footprint of  $12 \times 12 \mu\text{m}^2$ , and is set to have mirror symmetry along both horizontal and vertical directions, since the  $x$ - and  $y$ -crystal orientations are isotropic in our  $z$ -cut LNOI wafer. The objective function is designed to maximize the output power in fundamental  $\text{TE}_0$  mode. Here the minimum feature size is set to be  $0.5 \mu\text{m}$  as this optimization problem is easier to converge. Figure 3(b) shows the SEM image of the fabricated waveguide crossing. The simulated average insertion loss over a 100-nm wavelength band (Fig. 3(c)) is 0.22 dB, with low crosstalk of less than -40 dB. In the experiment, we measure the insertion loss by cascading five and twenty crossing structures and comparing with a single waveguide crossing (as indicated in the inset of Fig. 3(d)), showing a low fitted average insertion loss of 0.48 dB per crossing over the tested wavelength range (1500-1600 nm). The crosstalk values measured from the two vertical output waveguides (port 3 and port 4, Fig. 3(d)) are -36 dB and -39 dB, respectively, consistent with the simulation results. Similar to the top and bottom features in the mode multiplexer, we find that the corners of the design region also do not influence much on the device function (see Fig. S3(c-d) in S.I).

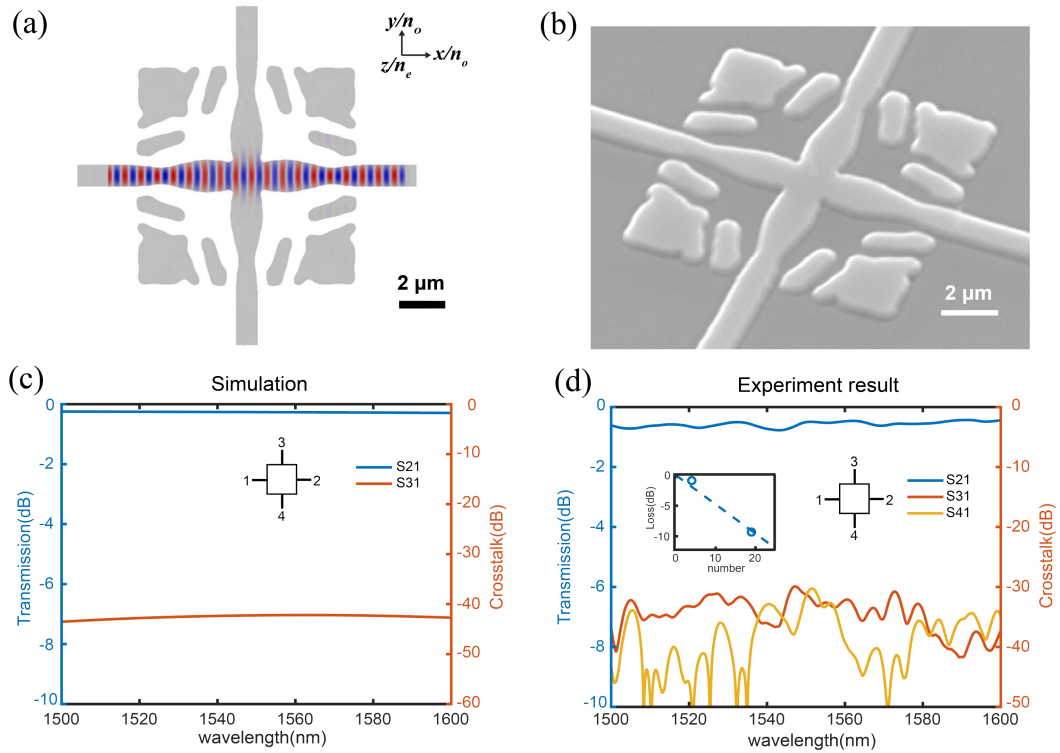


**Figure 3.** Inverse-designed LNOI waveguide crossing. (a) The optimized design pattern and simulated field ( $E_y$ ) evolution of the waveguide crossing with a  $12 \times 12 \mu\text{m}^2$  footprint. The gray and white areas correspond to LN rib and slab regions, respectively. (b) SEM image of the fabricated crossing device. (c) Simulated optical transmission ( $S_{21}$ ) and crosstalk ( $S_{31}$ ) of the designed waveguide crossing. (d) Experimentally measured device performance, showing a low insertion loss and crosstalk from 1500 nm to 1600 nm. Inset shows cut-back loss measurement results of 5 and 20 cascaded crossing structures.

## Compact waveguide bend



Finally, we demonstrate a compact bending waveguide that rotates the propagation direction of the fundamental  $TE_0$  mode by  $90^\circ$  within a tight bending radius of  $6\ \mu\text{m}$ . Due to the existence of unetched slab, waveguide bends in LNOI platforms usually require radii of at least  $30\ \mu\text{m}$  to limit the radiation loss. A simple circular  $90^\circ$  bend with a radius of  $6\ \mu\text{m}$  in our current platform will lead to a high loss of  $3.7\ \text{dB}$  according to our numerical simulation. Here the design region (Fig. 4(a)) is  $10 \times 10\ \mu\text{m}^2$  which is nearly an order of magnitude smaller than a traditional  $30\text{-}\mu\text{m}$  bend, both widths of input and output waveguides are  $1\ \mu\text{m}$ , and the minimum length scale is  $0.4\ \mu\text{m}$ . Figure 4(b) shows the SEM image of the fabricated waveguide bend. Physically, this optimized bend design could be roughly interpreted as a sharp bend augmented with a Bragg-mirror-like structure to suppress radiation loss, qualitatively similar to bends designed by topology optimization in other material platforms<sup>(57)</sup>, but determining the precise details requires the power of inverse design. The simulated average transmission loss (Fig. 4(c), blue) in the desired band ( $1500\ \text{nm} \sim 1600\ \text{nm}$ ) is  $0.29\ \text{dB}$ , which is equivalent to a simple bend with a radius of  $30\ \mu\text{m}$  according to our simulation. In the experimental test, we cascaded two, four, and six bends and compare the measured total insertion losses with a reference waveguide (Fig. 4(c), red and inset). The average measured insertion loss for a single bend is  $0.41\ \text{dB}$  over the  $100\text{-nm}$  wavelength range. The measured loss is slightly higher than expected, possibly due to an under-etched rib height ( $\sim 230\ \text{nm}$ ) resulting in more power leakage through the thicker slab. Nevertheless, the measured loss is still more than 8 times lower than that of a simple circular bend with the same radius.

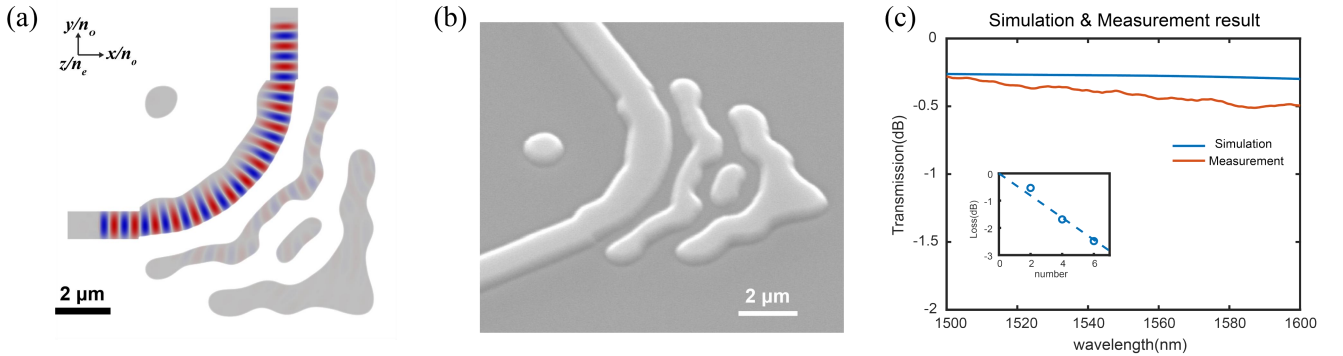


**Fig. 4.** Inverse-designed LNOI waveguide bend. (a) The optimized design pattern and simulated field ( $H_z$ ) evolution of the bending waveguide with a  $6\text{-}\mu\text{m}$  radius. The gray and white areas correspond to LN rib and slab regions, respectively. (b) SEM image of the fabricated waveguide bend. (c) Simulated and experimentally measured optical transmission of the waveguide bend, showing a low average insertion loss from  $1500\ \text{nm}$  to  $1600\ \text{nm}$ . Inset shows cut-back loss measurement results of two, four and six cascaded bends.

## Discussion

In summary, we have successfully implemented an inverse-design algorithm which is compatible with the practical fabrication constraints in the LNOI platform, including non-vertical sidewalls, relatively large minimum length scales and an unetched-slab structure. Based on this algorithm, we demonstrate, for the first time, a series of inverse-designed LNOI devices with small footprints, low losses, low crosstalk, broad bandwidths, and good consistency with theoretical prediction. Further relaxing the minimum length constraints could lead to designs compatible with stepper photolithography processes<sup>(58)</sup> with much better scalability and cost-effectiveness. The same design methodology could be readily applied to achieve LNOI devices with more advanced functions, especially those make use of the electro-optic and/or nonlinear properties of LN, such as fast-tunable switches<sup>(17)</sup>, dispersion-engineered comb generators<sup>(8)</sup>, and efficient nonlinear wavelength

convertors<sup>(10)</sup>, and be extended to other material platforms that share similar fabrication constraints, such as yttrium orthovanadate<sup>(59)</sup> and titanium dioxide<sup>(60)</sup>. The devices, together with the design methods, could become important building blocks for future LNOI functional photonic circuits with applications in on-chip optical links, quantum technologies and nonlinear optics.

## Acknowledgement

We thank Dr. Wenzhao Sun for valuable discussions on the manuscript.

## Funding:

National Natural Science Foundation of China (61922092),  
Research Grants Council, University Grants Committee (CityU 11204820, CityU 11212721, N\_CityU113/20),  
Croucher Foundation (9509005),  
Simons Foundation.

**Competing interests:** Authors declare that they have no competing interests.

## References

- (1) Zhu, D. et al., "Integrated photonics on thin-film lithium niobate," *Adv. Opt. Photon.*, vol. 13, pp. 242-352, 2021.
- (2) Wang, C. et al., "Integrated lithium niobate electro-optic modulators operating at CMOS-compatible voltages," *Nature*, vol. 562, pp. 101–104, Sep. 2018.
- (3) Xu, M. et al., "High-performance coherent optical modulators based on thin-film lithium niobate platform," *Nat. Commun.*, vol. 11, 2020.
- (4) Feng, H. et al., "Ultra-high-linearity integrated lithium niobate electro-optic modulators," *Photon. Res.*, vol. 10, pp. 2366-2373, 2022.
- (5) Zhang, M. et al., "Monolithic ultra-high-Q lithium niobate microring resonator," *Optica* vol. 4, pp. 1536-1537, 2017.
- (6) Liang, H.; Luo, R.; He, Y.; Jiang, H.; Lin, Q. "High-quality lithium niobate photonic crystal nanocavities," *Optica* vol. 4, pp. 1251-1258, 2017.
- (7) Wang, C. et al., "Monolithic lithium niobate photonic circuits for Kerr frequency comb generation and modulation," *Nat Commun.*, vol. 10, Feb. 2019.
- (8) Zhang, M. et al., "Broadband electro-optic frequency comb generation in a lithium niobate microring resonator," *Nature*, vol. 568, pp. 373-377, March, 2019.
- (9) He, Y. et al., "Self-starting bi-chromatic LiNbO<sub>3</sub> soliton microcomb," *Optica*, vol. 6, pp. 1138-1144, 2019.
- (10) Ledezma, L. et al., "Intense optical parametric amplification in dispersion-engineered nanophotonic lithium niobate waveguides," *Optica*, vol. 9, pp. 303-308, 2022.
- (11) Wang, C. et al., "Ultrahigh-efficiency wavelength conversion in nanophotonic periodically poled lithium niobate waveguides," *Optica*, vol. 5, pp. 1438-1441, 2018.
- (12) Lu, J. et al., "Periodically poled thin-film lithium niobate microring resonators with a second-harmonic generation efficiency of 250,000%/W," *Optica*, vol. 6, pp. 1455-1460, 2019.
- (13) Chen, J. Y. et al., "Ultra-efficient frequency conversion in quasi-phase-matched lithium niobate microrings," *Optica*, vol. 9, pp. 1244-1245, 2019.
- (14) Zhao, J.; Ma, C.; Rüsing, M.; Mookherjee, S. "High Quality Entangled Photon Pair Generation in Periodically Poled Thin-Film Lithium Niobate Waveguides," *Phys. Rev. Lett.*, vol. 124, April, 2020.



- 297 (15) Pohl, D. et al., "An integrated broadband spectrometer on thin-film lithium niobite," *Nat.*  
298 *Photonics*, vol. 14, pp. 24–29, 2020.
- 299 (16) Herrmann, J.F. et al., "Mirror symmetric on-chip frequency circulation of light," *Nat. Photon*,  
300 vol. 16, pp. 603–608, 2022.
- 301 (17) Guo, Q. et al., "Femtojoule femtosecond all-optical switching in lithium niobate nanophotonics,"  
302 *Nat. Photon*, vol. 16, pp. 625–631, 2022.
- 303 (18) Hu, Y. et al., "On-chip electro-optic frequency shifters and beam splitters," *Nature*, vol. 599, pp.  
304 587–593, 2021.
- 305 (19) Molesky, S. et al., "Inverse design in nanophotonics," *Nature Photon*, vol. 12, pp. 659–670, Oct.  
306 2018.
- 307 (20) Jensen, J.S.; Sigmund, O. "Topology optimization for nano-photonics," *Laser & Photon. Rev*,  
308 vol. 5, pp. 308–321, 2011.
- 309 (21) Borel, P. et al. "Imprinted silicon-based nanophotonics," *Opt. Express*, vol. 15, pp. 1261–1266,  
310 2007.
- 311 (22) Jensen, J.S.; Sigmund, O. "Systematic design of photonic crystal structures using topology  
312 optimization: Low-loss waveguide bends", *Appl. Phys. Let*, vol. 84, pp. 2022–2024, 2004.
- 313 (23) Borel, P.; Harpøth, A.; Frandsen, L.H.; Kristensen, M.; Shi, P.; Jensen, J.S.; Sigmund, O.  
314 "Topology optimization and fabrication of photonic crystal structures," *Opt. Express*, vol. 12, pp.  
315 1996–2001, 2004.
- 316 (24) Lu, J.; Vučković, J. "Nanophotonic computational design," *Opt. Express*, vol. 21, pp.  
317 13351–13367, 2013.
- 318 (25) Shen, B.; Wang, P.; Polson, R.; and Menon, R. "An integrated-nanophotonics polarization  
319 beamsplitter with  $2.4 \times 2.4 \mu\text{m}^2$  footprint," *Nature Photon*, vol. 9, pp. 378–382, May. 2015.
- 320 (26) Piggott, A. et al., "Inverse design and demonstration of a compact and broadband on-chip  
321 wavelength demultiplexer," *Nature Photon*, vol. 9, pp. 374–377, May. 2015.
- 322 (27) Piggott, A. et al., "Inverse design and implementation of a wavelength demultiplexing grating  
323 coupler," *Sci Rep*, vol. 4, Nov. 2014.
- 324 (28) Bayati, E. et al., "Inverse Designed Metalenses with Extended Depth of Focus," *ACS Photonics*,  
325 vol. 7, pp. 873–878, 2020.
- 326 (29) Sitawarin, C.; Jin, W.; Lin, Z.; Rodriguez, A. "Inverse-designed photonic fibers and  
327 metasurfaces for nonlinear frequency conversion [Invited]," *Photon. Res*, vol. 6, pp. B82–B89,  
328 2018.
- 329 (30) Lin, Z. et al., "Cavity-enhanced second-harmonic generation via nonlinear-overlap  
330 optimization," *Optica*, vol. 3, pp. 233–238, 2016.
- 331 (31) Christiansen, R.E. et al., "Inverse design of nanoparticles for enhanced Raman scattering," *Opt.*  
332 *Express*, vol. 28, pp. 4444–4462, 2020.
- 333 (32) Ahn, G. et al., "Photonic Inverse Design of On-Chip Microresonators," *ACS Photonics*, vol. 9,  
334 pp. 1875–1881, 2022.
- 335 (33) Yang, J.; Yang, K.Y.; Guidry, M.A.; Lukin, D. M.; Vuckovic, J. "Inverse-Designed Silicon  
336 Carbide Nanoresonators," in *Conference on Lasers and Electro-Optics*, Technical Digest Series  
337 (Optica Publishing Group, 2022), paper STh4F.4.
- 338 (34) Yang, K.Y. et al., "Inverse-designed multi-dimensional silicon photonic transmitters," 2021,  
339 *arxiv*: 2103.14139.
- 340 (35) Sapra, N.V. et al., "On-chip integrated laser-driven particle accelerator," *Science*, vol. 367, pp.  
341 79–83, 2020.
- 342 (36) Yang, K.Y. et al., "Inverse-designed non-reciprocal pulse router for chip-based LiDAR," *Nat.*  
343 *Photonics*, vol. 14, pp. 369–374, 2020.
- 344 (37) Vercruyssen, D.; Sapra, N. V.; Yang, K. Y.; Vučković, J. "Inverse-Designed Photonic Crystal  
345 Circuits for Optical Beam Steering," *ACS Photonics*, vol. 8, pp. 3085–3093, 2021.

- (38) Hammond, A.M. et al., "Photonic topology optimization with semiconductor-foundry design-rule constraints," *Opt. Express*, vol. 29, pp. 23916-23938, 2021.
- (39) Pan, Y. et al., "Topology optimization of surface-enhanced Raman scattering substrates," *Appl. Phys. Lett*, vol. 119, 061601, 2021.
- (40) Christiansen, R.E. et al. "Creating geometrically robust designs for highly sensitive problems using topology optimization," *Struct Multidisc Optim*, vol. 52, pp. 737-754, 2015.
- (41) Schevenels, M.; Lazarov, B.S.; Sigmund, O. "Robust topology optimization accounting for spatially varying manufacturing errors," *Computer Methods in Applied Mechanics and Engineering*, vol. 200, pp. 3613-3627, 2011.
- (42) Piggott, A. et al., "Inverse-Designed Photonics for Semiconductor Foundries," *ACS Photonics*, vol. 7, pp. 569-575, 2020.
- (43) Dory, C. et al., "Inverse-designed diamond photonics," *Nat Commun*, vol. 10, 3309, 2019.
- (44) Oskooi, A. et al., "MEEP: A flexible free-software package for electromagnetic simulations by the FDTD method," *Computer Physics Communications*, vol. 181, pp. 687-702, 2010.
- (45) Hammond, A.M. et al., "High-performance hybrid time/frequency-domain topology optimization for large-scale photonics inverse design," *Optics Express*, vol. 30, pp. 4467-4491, 2022.
- (46) Chen, Z.; Yang, J.; Wong, W.; Pun, Y.; Wang, C. "Broadband adiabatic polarization rotator-splitter based on a lithium niobate on insulator platform," *Photon. Res*, vol. 9, pp. 2319-2324, 2021.
- (47) Zhou, M.; Lazarov, B.S.; Wang, F.; Sigmund, O. "Minimum length scale in topology optimization by geometric constraints," *Computer Methods in Applied Mechanics and Engineering*, vol. 293, pp. 266-282, Aug. 2015.
- (48) Luo, L.W. et al., "WDM-compatible mode-division multiplexing on a silicon chip," *Nat Commun*, vol. 5, 3069, 2014.
- (49) Liu, Y. et al., "On-chip four-mode (de-)multiplexer on thin film lithium niobate-silicon rich nitride hybrid platform," *Opt. Lett*, vol. 46, pp. 3179-3182, 2021.
- (50) Zhang, M. et al., "Electro-optic reconfigurable two-mode (de)multiplexer on thin-film lithium niobate," *Opt. Lett*, vol. 46, pp. 1001-1004, 2021.
- (51) Manolatou, C. et al., "High-Density Integrated Optics," *J. Lightwave Technol*, vol. 17, pp. 1682-, 1999.
- (52) Johnson, M.; Thompson, M.G.; Sahin, D. "Low-loss, low-crosstalk waveguide crossing for scalable integrated silicon photonics applications," *Opt. Express*, vol. 28, pp. 12498-12507, 2020.
- (53) Nelan, S. et al., "Compact thin film lithium niobate folded intensity modulator using a waveguide crossing," *Opt. Express*, vol. 30, pp. 9193-9207, 2022.
- (54) Han, L.; Ruan, X.; Tang, W.; Chu, T. "Ultralow-loss waveguide crossing for photonic integrated circuits by using inverted tapers," *Opt. Express*, vol. 30, pp. 6738-6745, 2022.
- (55) Kim, S. et al., "Tilted MMI crossings based on silicon wire waveguide," *Opt. Express*, vol. 22, pp. 2545-2552, 2014.
- (56) Yi, D.; Zhou, W.; Zhang, Y.; Tsang, H. "Inverse design of multi-band and wideband waveguide crossings," *Opt. Lett*, vol. 46, pp. 884-887, 2021.
- (57) Tsuji, Y.; Hirayama, K. "Design of Optical Circuit Devices Using Topology Optimization Method With Function-Expansion- Based Refractive Index Distribution," *IEEE Photonics Technology Letters*, vol. 20, pp. 982-984, 2008.
- (58) Zhang, K. et al., "A power-efficient integrated lithium niobate electro-optic comb generator," *Commun. Phys*, vol. 6, 17, 2023.
- (59) Zhong, T. et al., "Nanophotonic rare-earth quantum memory with optically controlled retrieval," *Science*, vol. 357, pp. 1392-1395, 2017.

395 (60) Wu, Y. et al., "TiO2 metasurfaces: From visible planar photonics to photochemistry," *Science*  
396 *advances*, vol. 5, 2019.

397  
398  
399

400 For Table of Contents Use Only

401  
402  
403  
404  
405

406 **Title**

407 Inverse-designed lithium niobate nanophotonics

408

409 **Authors**

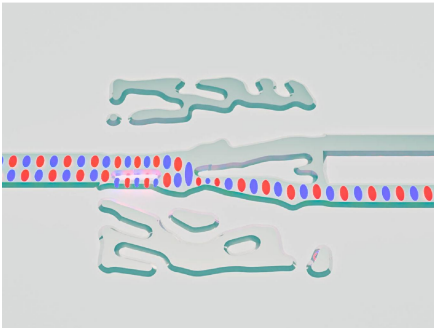
410 Chengfei Shang, Jingwei Yang, Alec M. Hammond, Zhaoxi Chen, Mo Chen, Zin Lin, Steven G.  
411 Johnson, and Cheng Wang

412

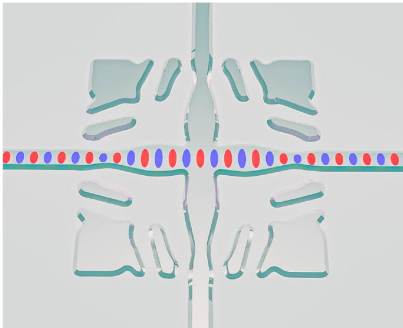
413

414 **Table of Contents (TOC) Graphic**

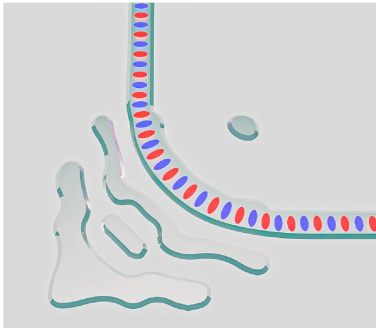
LNOI



Mode multiplexer



Waveguide crossing



Waveguide Bend

415  
416

417

418 **Brief synopsis**

419 The TOC graphic shows the schematic views of our LNOI designed structures and their  
420 corresponding functionalities.

421

422